Energy 206 (2020) 118096

Contents lists available at ScienceDirect

Energy

journal homepage: www.elsevier.com/locate/energy

Enhancing the performance of fully-scaled structure-adjustable 3D thermoelectric devices based on cold–press sintering and molding

Kai Liu [a], Xiaobin Tang [a, b, *], Yunpeng Liu [a, b], Zhiheng Xu [a, b], Zicheng Yuan [a], Zhengrong Zhang [a]

[a] Department of Nuclear Science and Technology, Nanjing University of Aeronautics and Astronautics, Nanjing, 210016, China
[b] Key Laboratory of Nuclear Technology Application and Radiation Protection in Astronautics, Nanjing University of Aeronautics and Astronautics, Ministry of Industry and Information Technology, China

ARTICLE INFO

Article history:
Received 13 February 2020
Received in revised form
2 June 2020
Accepted 8 June 2020
Available online 22 June 2020

Keywords:
Cold–press sintering and molding
Energy conversion
One–time forming
Structure-adjustable
Thermal conductivity
Thermoelectric device

ABSTRACT

The growing concern over the global energy crisis strengthened the research on thermoelectricity. It would be logical to prepare practical thermoelectric device to effectively utilize various low-quality heat. In this study, the high-performance structure-adjustable 3D thermoelectric devices were fabricated by cold-press sintering and molding technologies. The thermoelectric figures of merit (ZT) of pressurized P and N–type materials reached the maximum of 1.09 and 0.5 at room temperature, respectively. The holes introduced by the binder and pressurization process reduced thermal conductivity and enhanced electrical properties. The in–depth influence on the thermoelectric devices was shown via simulation calculation. Fully-scaled thermoelectric devices suitable for various occasions were fabricated by one–time forming. The tandem of small and large arrayed thermoelectric devices respectively generated open–circuit voltages (V_{oc}) of 584 mV and 573.8 mV and maximum output powers (P_{max}) of 627.7 μW and 1.2 mW at 398.15 K. The V_{oc} values of arched and annular thermoelectric devices were 265 mV and 332.1 mV at 398.15 K, respectively, and the P_{max} values were 948.5 μW and 1.2 mW, respectively. On account of its good structure adjustability and high performance, thermoelectric devices fabricated will be broadly applied in solar–thermal conversion systems, automotive heat reclaimer and radioisotope thermoelectric generator.

1. Introduction

In order to overcome the global energy crisis and adhere to sustainable development, it is urgently needed to seek for alternative method to utilize tremendous low–quality heat in nature. Thermoelectric devices [1], which convert heat energy into electricity by using the Seebeck effect, have the merits of static conversion, free of noises or greenhouse emission, vast scalability for multiple application [2,3]. Hence, it is an appealing option of sustainable utilization. At present, thermoelectric devices are extensively used to power generation in various fields, such as solar–thermal conversion systems [4], implantable or wearable devices [5,6], automotive heat reclaimer [7], and others. It are also employed as temperature sensors and controllers for electrical engineering [8,9]. Moreover, space electronic components [10], robotic exploration packages [11], and planetary exploration [12] are quite a bit supplied by radioisotope thermoelectric generators (RTGs).

The performance of thermoelectric devices in practical applications is largely dependent on the preparation methods of thermoelectric materials and devices. Firstly, the hot–press sintering and welding method is generally used to prepare 3D thermoelectric devices [13–15]. Using this method, Zhang et al. [16,17] achieved a thermoelectric conversion efficiency of 12% and a power density of 1.4 W cm^{-2} under a temperature difference of 541 K in the harvesting of waste industrial heat. Aranguren et al. [18] obtained 21.56 W of net energy with 48 thermoelectric modules to recover waste heat from a combustion chamber. Extra attention now has been devoted to the high proportion of materials damaged by secondary processing. The entire device is too dispersed to be accomplished at one time. Moreover, the flat-type device made by this method does not match well with all heat sources, which bring

* Corresponding author. Department of Nuclear Science and Engineering, Nanjing University of Aeronautics and Astronautics, Nanjing, 211106, China.
E-mail address: tangxiaobin@nuaa.edu.cn (X. Tang).

https://doi.org/10.1016/j.energy.2020.118096
0360-5442/

Nomenclature

A_1	The heat-receiving area, mm^2
C	Stefan–Boltzmann constant
C_d	Heat capacity at constant volume
d	Mean free path of the phonon
e	Carrier charge, C
F_{ab}	view factor
h	Planck constant
h_c	Convective heat transfer coefficient, $W \cdot m^{-2} \cdot K^{-1}$
J	Current density
K_B	Boltzmann constant
L	Lorentz constant
l	Length of the thermoelectric leg, mm
m^*	Effective mass
n	Carrier concentration, cm^{-3}
N	Number of thermocouples
P_{max}	Maximum output power of the RTG, W
P_{out}	Output power of the RTG, W
Q	Energy accumulation
Q_{rad}	Net heat radiation from surface to surface
q	Heat flux of the thermoelectric leg, $W \cdot m^{-2}$
q_0	Convective heat flux, $W \cdot m^{-2}$
R	External load resistance in the RTG, Ω
r	Internal resistance in the RTG, Ω
S	Cross-sectional area of a single P-type or N-type leg, mm^2
V	Output voltage of the RTG, V
V_{oc}	Open–circuit voltage of the RTG, V
ZT	Figure of merit of thermoelectric materials
ΔT	Temperature difference of both sides of thermoelectric devices, K
σ	Electrical conductivity, $S \cdot m^{-1}$
α	Seebeck coefficient, $V \cdot K^{-1}$
κ	Thermal conductivity, $W \cdot m^{-1} \cdot K^{-1}$
κ_L	Lattice thermal conductivity, $W \cdot m^{-1} \cdot K^{-1}$
κ_e	Carrier thermal conductivity, $W \cdot m^{-1} \cdot K^{-1}$
ν	Diffusion rate of the phonon
μ	Carrier mobility, $cm^3 \cdot V^{-1} \cdot s^{-1}$
ρ	Density of thermoelectric materials, $g \cdot cm^{-3}$
ε	Emissivity coefficient

irreconcilable difficulties to the practical heat utilization. Secondly, the screen printing method is another major topic of discussion [19,20]. On the basis of screen printing technique, Varghese et al. [21] produced flexible thermoelectric films with a power density of 4.1 mW cm^{-2} in energy harvesting and cool applications. Choi et al. [22,23] fabricated a thin–film thermoelectric device with a high output power density of 5.02 mW cm^{-2} – 5.45 mW cm^{-2}, which can be applied to non–flat surfaces. These works demonstrated the feasibility of mass printing thermoelectric devices with good reliability and reproducibility, but their thermoelectric performance still have a great margin for improvement. Thirdly, sputtering [24], electro deposition [25], and 3D printing methods [26], which have gradually became the focus of research, are also available. Son et al. [27,28] developed all–inorganic thermoelectric inks with ZT values of 0.9 (P–type) and 0.6 (N–type) for 3D printing. These inks enabled the fabrication of thermoelectric materials with different geometries. Although these methods have the advantages of accurate preparation and low porosity, the improved process and low cost of widespread application need be imperative consideration. Therefore, an efficient and pragmatic method for fabricating high–performance 3D thermoelectric devices that satisfy unique requirements is currently lacking.

This manuscript discusses electric energy harvesting from heat sources based on thermoelectric energy harvesters. In this manner, this paper proposes a high-performance and structure-adjustable 3D thermoelectric device fabricated through a combination of cold-press sintering and molding technologies, by introducing ultralow thermal conductivity (as low as 0.2 W m^{-1} K^{-1}). This commendably solves complicated problems of high breakage rate, and small temperature difference, and thereby effectively improves energy efficiency and output power of the thermoelectric generators. The fabricated thermoelectric generator targets applications such as solar-thermal conversion systems, automotive heat reclaimers, and radioisotope thermoelectric generators. The paper presents four configurations of 3D thermoelectric generators, which are small and large arrayed thermoelectric plates and single curved and annular thermoelectric configurations. In the analysis, based on the microstructure and atomic levels of materials, several material properties analyses of the fabricated P and N-type materials are made, including XRD and SEM analyses for pressurized and unpressurized P/N materials. Parametrical analyses of the generated electricity versus the material properties are performed based on simulations using the COMSOL platform. Thereafter, considering an electric heating test rig, the performance of the proposed thermoelectric generators is tested using a low-quality heat with a temperature ranged from 323.15 K to 398.15 K.

2. Experimental section

2.1. Cold–press sintering and molding method

This method was utilized to prepare good thermoelectric material with low thermal conductor by cold pressing and sintering, and fabricate complicated 3D thermoelectric devices with excellent electrical output by molding. The usual preparation process is shown in Fig. 1. Firstly, thermoelectric paints were disposed and filled into a mold (Fig. 1(a and b). The P/N Bi_2Te_3-based powder doped with Sb or Se was mixed with DER732 binder (polypropylene glycol diglycidyl ether) at a mass ratio of 88:12. Second, the filled mold was placed in the press machine under 30 MPa cold–pressing pressures (Fig. 1(c)). This operation effectively increased the tightness of the materials. The P/N thermoelectric leg can be connected by pressing the paint without additional electrode material. Third, the thermoelectric devices after demolding (Fig. 1(d and e)) were sintered at 573.15 K for 3.5 h Der732 contained a variety of binders and diluents. By adjusting the mass ratio of the thermoelectric powder to Der732, pressure, and sintering temperature, the molecular connection and crystallization of material were changed, which are reflected on the electrical properties of the material on a macro scale. PDMS sealant was then used to seal the thermoelectric devices (Fig. 1(f)). After removing the partial sealant, the two electrodes were electroplated with nickel/tin electrodes, and the thermoelectric devices were connected in series by welding (Fig. 1(g and h)). This work combined the method of

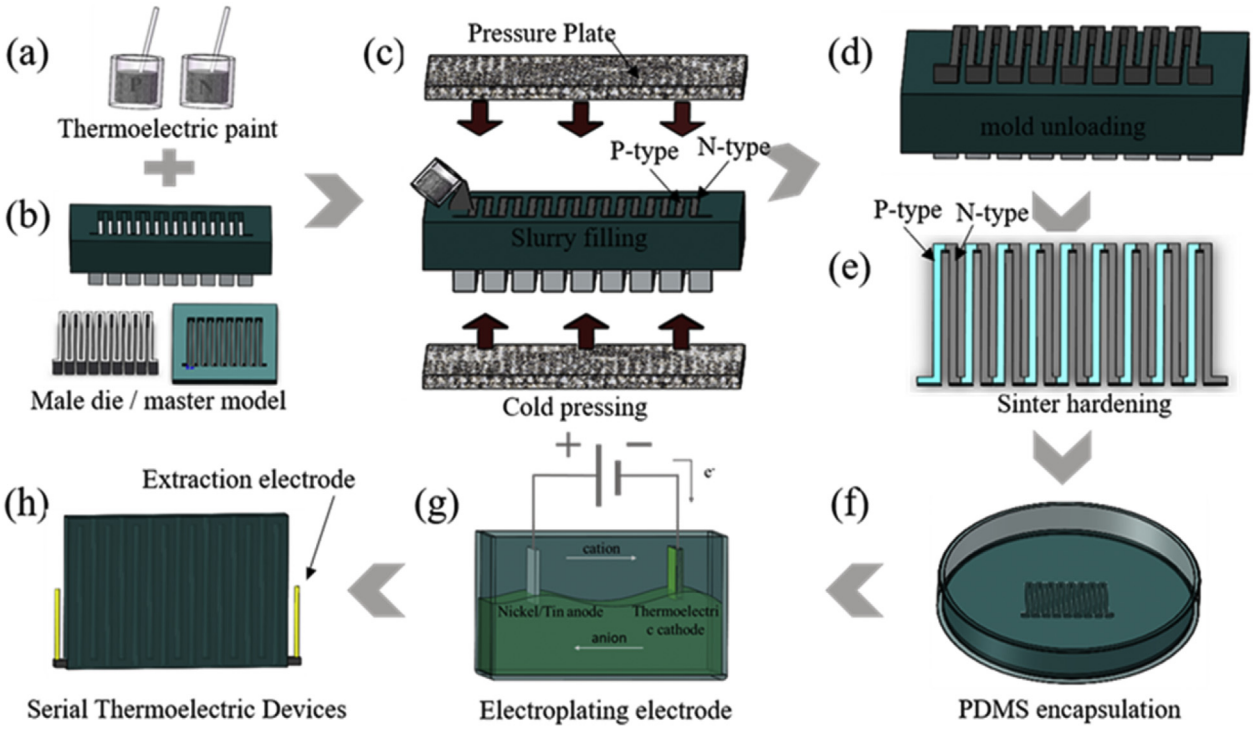

Fig. 1. Fabrication of thermoelectric devices based on cold–press sintering and molding method.

molding with cold–press sintering ingeniously and achieved the one–time forming of thermoelectric devices. This method addressed the problem of brittleness and waste in processing thermoelectric materials, which greatly improve the fabrication process and thermoelectric performance of devices. Through designing the structure and size of the mold used, various 3D thermoelectric legs and devices can be developed for different heat sources, temperature ranges and dimensions according to application requirements.

2.2. Characterization of thermoelectric materials

For degenerate Bi_2Te_3-based semiconductors (parabolic band, energy-independent scattering approximation), the interrelationship between carrier concentration (n), effective mass (m^*) and Seebeck coefficient (α) can be observed in relatively simple models of electron transport. The electrical conductivity (σ) is linked to n through the carrier mobility (μ). The thermal conductivity (κ) mainly originates from two parts: (1) phonons travelling through the lattice (κ_l) and (2) electrons and holes transporting heat (κ_e). To maximize the thermoelectric figure of merit (ZT) of a material, a large α, high σ, and low κ are required.

$$\alpha = \frac{8\pi T m^* K_B^2}{3eh^2}\left(\frac{\pi}{3n}\right)^{\frac{2}{3}} \tag{1}$$

$$\sigma = en\mu \tag{2}$$

$$\kappa = \kappa_L + \kappa_e = \frac{C_v v d}{3} + L\sigma T \tag{3}$$

$$ZT = \frac{\alpha^2 \sigma}{\kappa} T \tag{4}$$

where K_B, h, and L represented the Boltzmann, Planck, and Lorentz constants, respectively. T was the temperature, and q was the carrier charge.

The cold–pressing pressure played a noteworthy role in the material preparation. The advantages of materials prepared were compared through a control experiment with or without cold–pressing pressure of 30 MPa. P/N block samples were prepared by particular molds. The effects of the pressurization process on material morphology and thermoelectric performance were also discussed. The morphology and composition of the samples were characterized by scanning electron microscopy (SEM) and X–ray powder diffraction (XRD), respectively. The thermoelectric parameters of the materials at different temperatures were measured with a thermoelectric parameter measurement system (Namicro–3), Hall effect testing system (HT–50 type), and thermal conductivity tester (DRL–III). Considering energy conversion of low-quality heat applications and Bi_2Te_3–based materials suitable for the low–temperature situation, the fabricated thermoelectric materials were tested under relevant temperature ranges of 323.15 K–398.15 K.

2.3. Finite element analysis

The thermoelectric properties of P/N materials with or without pressurization have been analyzed. To analyze the effects of these properties on thermoelectric devices, a thermoelectric device model was built by using COMSOL software. The coupling analysis of heat transfer, current and thermoelectric effect was carried out. The current density (J) consists of Ohms law and the Seebeck effect. The heat flux (q) are composed of Fourier heat conduction and Peltier effect.

$$-J = \sigma \cdot \nabla V + \sigma \cdot \alpha \cdot \nabla T \tag{5}$$

$$q = -\kappa \cdot \nabla T + T \cdot \alpha \cdot J \tag{6}$$

The J was divergence-free in steady state, and the boundary condition was shown as follows:

$$\nabla \cdot J = 0 \tag{7}$$

$$q_0 = h_c(T_{ext} - T) \tag{8}$$

$$Q_{rad} = F_{ab} A_a \varepsilon c \left(T_b^4 - T_a^4\right) \tag{9}$$

And at this moment the energy accumulation (Q) must be 0:

$$Q = \nabla \cdot (\kappa \nabla T) - \nabla((V + T\alpha) * J) = 0 \tag{10}$$

The thermoelectric parameters of the P/N materials with and without pressurization were substituted into the models. By generating the tetrahedral mesh and solving the above equations, the steady-state electrical output of thermoelectric devices can be achieved. The electrical performance of the devices was simulated in heat source temperature ranged from 323.15 K to 398.15 K. The model structure of the thermoelectric devices is illustrated in Fig. 5(a and b). The size, including the length, width, and thickness of each thermoelectric leg, varies from the interval provided in Table 1. 8 pairs of P/N thermoelectric legs are included in the thermoelectric devices.

2.4. Performance test of thermoelectric devices

When the power or temperature of a heat source is stable, the internal relation between the electrical outputs of thermoelectric devices, such as open−circuit voltage (V_{oc}) and output power (P_{out}), and the parameters of the materials were established. The specific calculation equations are as follows:

$$V_{oc} = (\alpha_p - \alpha_n) \times \Delta T \times N \tag{11}$$

$$P_{out} = \frac{V^2}{(R + r)^2} \times R = \frac{(\alpha_p - \alpha_n) \cdot \Delta T \cdot N^2}{\left(R + \frac{\rho l}{S}\right)^2} \times R \tag{12}$$

where N was the number of thermocouples α_p and α_n are the Seebeck coefficients of P-type and N-type thermoelectric materials, respectively. P_{out} was the output power when the external resistance (R) of the devices is connected. The internal resistance of the thermoelectric devices (r) is intrinsically related to the size of thermoelectric legs. The maximum output power (P_{max}) can be obtained as $R = r$.

After the preparation of the thermoelectric devices, the electrical performances of the thermoelectric filaments were tested using a parameter analyzer (Keithley 4200 SCS) at 293.15 K ambient temperature. As revealed in Fig. 2, the electrical heating source provides a constant heat in a range of 323.15 K−398.15 K. It's equivalent to the low-quality heating sources, such as industrial wastewater, automobile exhaust, and solar energy. To minimize the error of the measurement data, the samples were processed after heating them for half an hour. The real−time temperatures of the hot and cold sides of the thermoelectric devices were measured with a temperature sensor (R7100).

Table 1
Relevant dimensions of thermoelectric devices in COMSOL.

Thermoelectric leg	Variety range
Length (mm)	5−20
Width (mm)	0.5−2
Thickness (mm)	0.5−2
Quantity (pair)	8

3. Characterization and analysis of thermoelectric materials

3.1. Atlas analysis of XRD and SEM images

Fig. 3(a) shows that the phases in the P/N thermoelectric materials are the same with and without pressurization. The phase of the P−type materials was $Bi_{0.5}Sb_{1.5}Te_3$, and that of the N−type materials was $Bi_2Se_{0.3}Te_{2.7}$. Fig. 3(b) illustrates abundant holes on the surface of the P/N thermoelectric materials, leading to a large number of grain boundaries and defects. This phenomenon was caused by the volatilization of the binder after sintering. As a result, the κ values of the thermoelectric materials were one order of magnitude lower than that of commercial thermoelectric materials (Fig. 4(c)). The density values (ρ) of the four materials are obtained and shown in Table 2. The density of the pressurized thermoelectric materials was greater than that of the unpressurized ones. The pressure treatment makes the thermoelectric materials compact. In the light of the adhesion theory of binders, the intermolecular Brownian motion was aggravated by the pressure, temperature, and low viscosity, then promoting the diffusion of bonding agent molecules to the interface of bismuth telluride molecules. This condition was conducive to the transport of carriers in the bonding system. Therefore, it eventually led to an improved electrical conductivity of pressurized thermoelectric materials (Fig. 4(b)).

3.2. Analysis of thermoelectric parameters

The performance curves of the P/N thermoelectric materials with or without pressurization (30 MPa) are presented in Fig. 4. The pressure treatment exerted minimal effect on α of the materials (Fig. 4(a)). The highest σ was at 298.15 K, then decreased with increasing temperature (Fig. 4(b)). The σ values of the pressurized P/N materials were significantly higher than those of the non−pressurized materials. The maximum σ values of the pressurized P and N−type materials were 1.24×10^4 S m^{-1} and 1.81×10^4 S m^{-1}, respectively. Even though the κ values of the pressurized materials were slightly higher than those of the unpressurized materials (Fig. 4(c)), the κ was still in a very low range from 0.2 W m^{-1} K^{-1} to 0.67 W m^{-1} K^{-1}). The extremely low k and commendable thermoelectric properties of the materials are mainly due to the addition of the binder. The ZT values of the pressurized thermoelectric materials were higher than those of the unpressurized materials (Fig. 4(d)). The maximum ZT values of the pressurized P/N thermoelectric materials reached 1.09 and 0.5 at room temperature and then decreased with increasing temperature. The variations of carrier concentration of P/N material were slightly before and after pressurization, while the mobility of the pressurized P/N thermoelectric materials was higher than those of

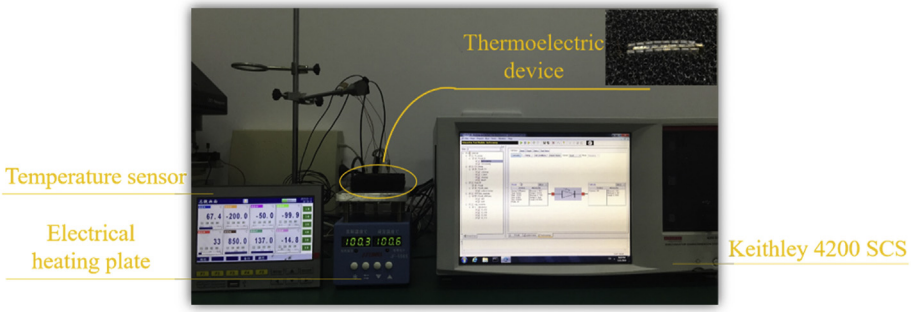

Fig. 2. Test chart of electrical performance of thermoelectric devices.

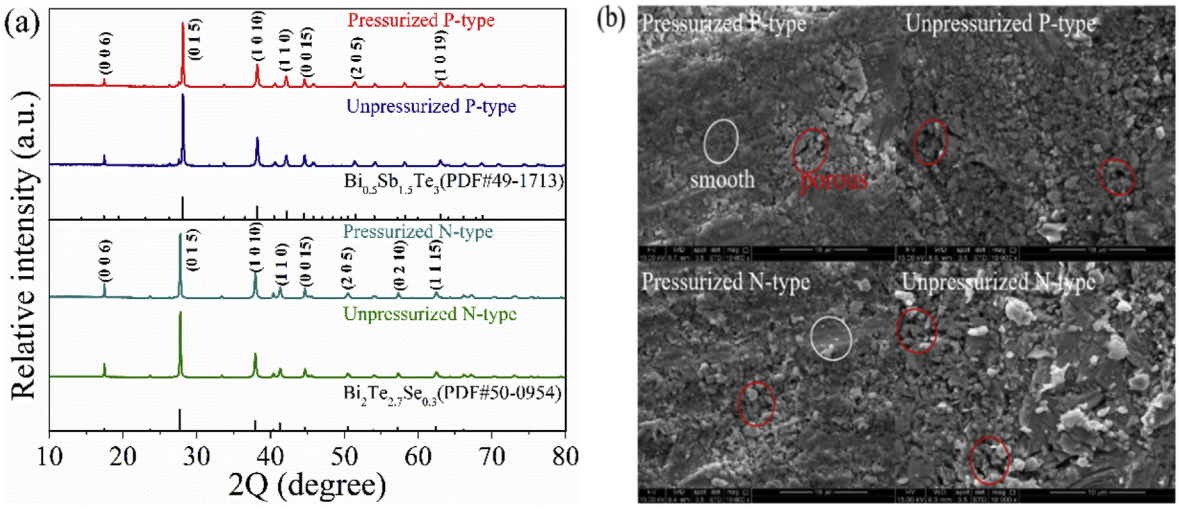

Fig. 3. Morphological and composition analyses of the P/N thermoelectric materials: (a) XRD spectrum, (b) SEM image.

the unpressurized thermoelectric materials (Fig. 4(e and f)). Therefore, as depicting in eq. (2), the increase of σ of the pressurized P/N materials was primarily put down to the improved material mobility obtained by compression technology. In addition, the decrease of mobility made the σ decrease with the increase of temperature. The increase in temperature aggravated the lattice scattering in the materials and then reduced the mobility of the materials. As the σ values of the materials decreased with increasing temperature, the carrier thermal conductivity in eq. (3) also declining. However, the κ values of the materials in Fig. 4(c) increased. So the lattice thermal conductivity increased with temperature, offsetting the effects of the reduced carrier thermal conductivity. The κ values of the materials prepared in the current work were one order lower than those of commercially mature Bi_2Te_3—based thermoelectric materials, whereas these α values exhibited minimal differences. Since the improvement of the κ was more than the reduction of the σ, the thermoelectric materials prepared in this work show favorable thermoelectric performances according to eq. (4).

4. Results and discussion

4.1. Simulation and contrastive analysis

The influence of material properties on the electrical performance of the devices under different sizes was comprehensively discussed. Fig. 5(a and b) shows the distribution of the temperature and potential fields of the thermoelectric devices with a dimension of $20 \times 1 \times 1$ mm^3 at a hot surface temperature of 398.15 K. The two end of thermoelectric devices showed a large temperature difference and good electrical performance. In Fig. 5(c–f), the V_{oc} values of the pressurized and unpressurized thermoelectric devices are slightly different at the same heat source temperature and size because pressure exerted a minimal effect on the Seebeck coefficient of the materials (Fig. 4(a)). Under the same conditions, the P_{max} values of the pressurized thermoelectric devices were far greater than those of the unpressurized thermoelectric devices. The pressurized thermoelectric devices obtained the maximum V_{oc} value of 305.3 mV and P_{max} of 2.28 mW, whereas the unpressurized thermoelectric devices obtained the maximum V_{oc} value of 304.5 mV and P_{max} of 410.7 μW. The internal resistance of the device was effectively reduced because the electrical conductivity of thermoelectric material was improved after pressurization. For example, the internal resistance of a thermoelectric device with a

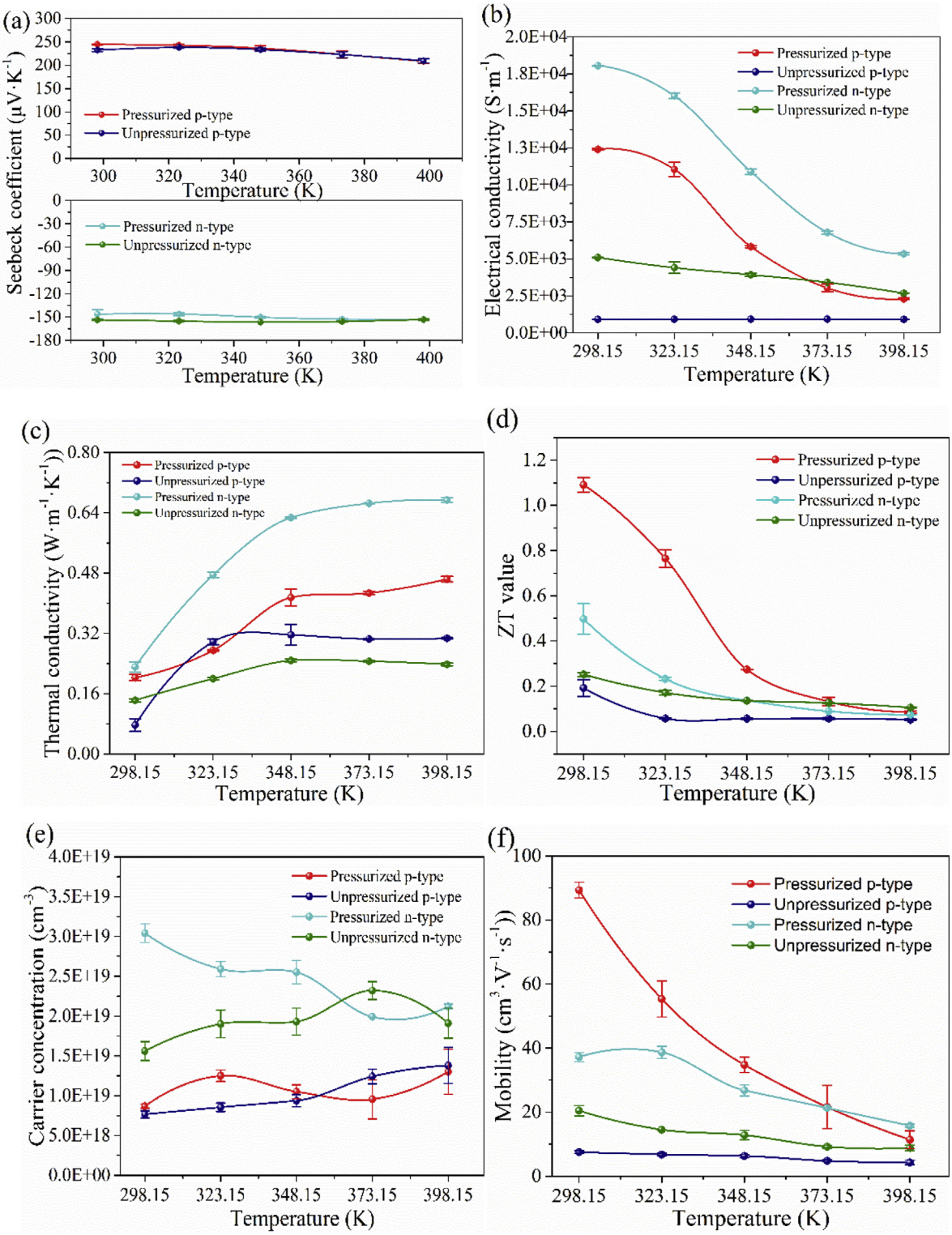

Fig. 4. Analysis of the thermoelectric performance criterion of P/N thermoelectric materials. (a) Seebeck coefficient, (b) electrical conductivity, (c) thermal conductivity, (d) figure of merit, (e) carrier concentration, (f) carrier mobility.

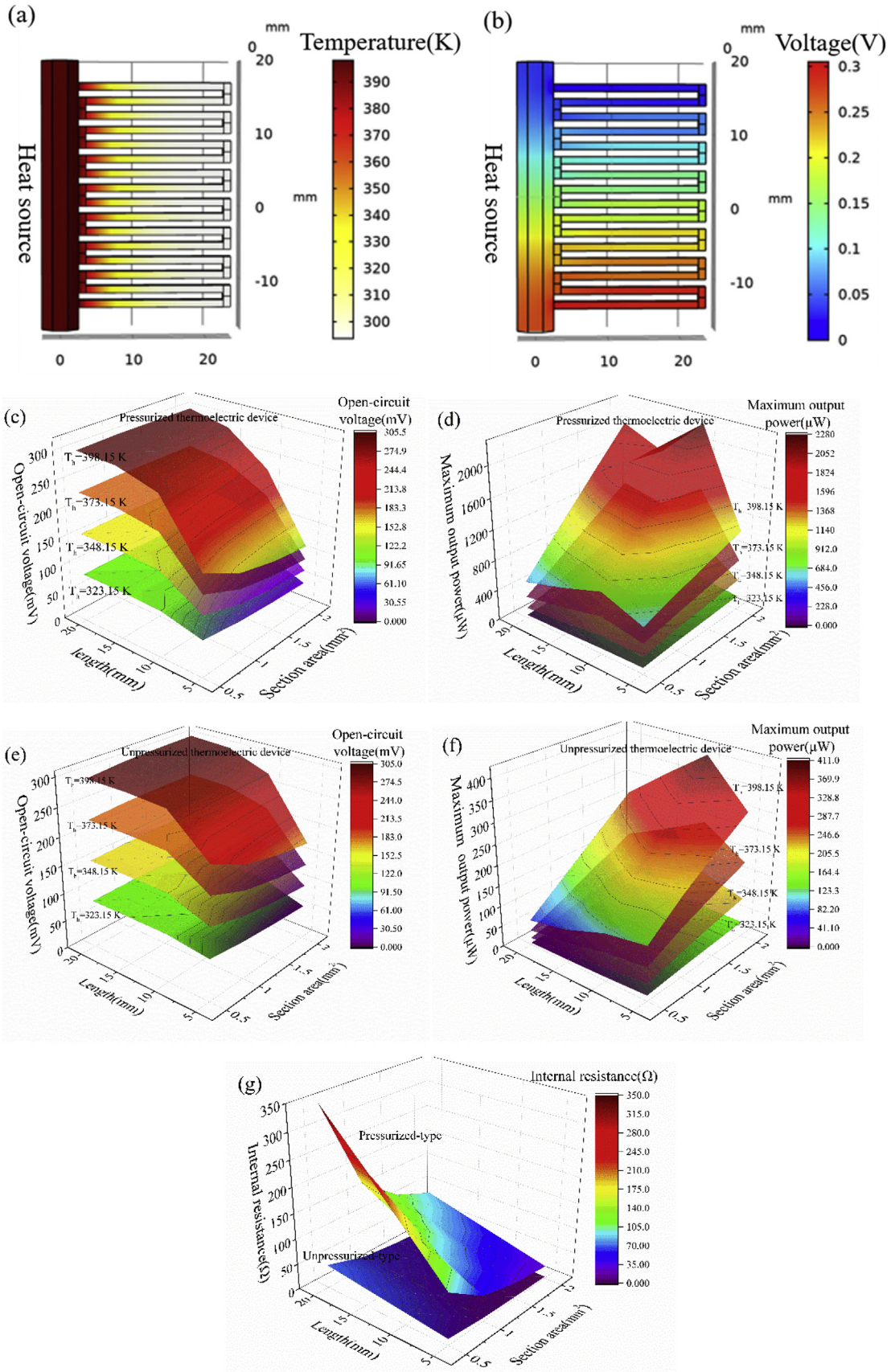

Fig. 5. Electrical performance of thermoelectric devices under different sizes: (a) temperature field distribution, (b) potential field distribution, (c–f) V_{oc} and P_{max} of pressurized and unpressurized thermoelectric devices (width of 1 mm), (g) internal resistance *r*.

Table 2
Density values of four thermoelectric materials.

Type	Density value ($g \cdot cm^{-3}$)
Pressurized P−type	5.14
Unpressurized P−type	4.39
Pressurized N−type	5.87
Unpressurized N−type	3.9

thermoelectric leg of 20 × 1 × 1 mm^3 is effectively reduced from 174.6 Ω to 22.9 Ω after pressurization, as shown in Fig. 5(g). When the V_{oc} values of the pressurized and unpressurized devices were not much different, the lower the internal resistances of the devices were, the higher the output power of the devices will be. The electrical output of the thermoelectric devices under other widths of the thermoelectric legs is shown in the supplementary materials (Supplementary Figs. S1−S4), and similar conclusions can be drawn. Those simulation results proved that pressurization does have promotion effects on improving device performance, which provides a worthy reference for subsequent device preparation.

4.2. Arrayed thermoelectric device

To ascertain that the practical performance of arrayed thermoelectric configuration, the 3D arrayed thermoelectric devices were fabricated with two different sizes by molding (Fig. 6(a)). The exact sizes are shown in Table 3. Three thermoelectric devices were connected in series by electrode welding and then tested under the plane heat source in the temperature range of 323.15 K−398.15 K to evaluate the ability of the devices to collect low−quality waste heat.

The internal resistance values of the small and large thermoelectric devices in series were 119.5 Ω and 71.3 Ω at room temperature, respectively. With increasing heat source temperature, the electrical performance of the devices increased. When the hot surface temperature was 398.15 K, the V_{oc} and P_{max} of the small thermoelectric devices reached 584 mV and 627.7 μW, respectively, as shown in Fig. 6(c and d). The temperature difference (ΔT) between the two ends of the devices reached 75.7 K. In Fig. 6(e and f), the V_{oc}, P_{max}, and ΔT of the large thermoelectric devices are 573.8 mV, 1.2 mW, and 72.8 K under the same conditions, respectively. The small and large thermoelectric devices showed almost the same output voltages mostly because of those similar $\triangle T$. However, the large devices presented minimal internal resistance and good output power for their large cross−sectional area. These results are also consistent with the simulation. The small devices can be applied to surface heat sources by using PDMS sealant (Fig. 6(b)). The thermoelectric devices were tested given a curved heat source of a 5 cm diameter and temperature range of 323.15 K−398.15 K. At 398.15 K heat source temperature, the V_{oc}, P_{max}, and ΔT of the thermoelectric devices reached 668 mV, 700.5 μW, and 86.5 K, respectively (Fig. 6(g and h)). The results were comparable to the electrical output of the devices under a plane heat source. Therefore, the 3D arrayed thermoelectric devices are capable of collecting low−quality heat in various occasions. It can be applied to not only flat collectors to collect sunlight, but also curved water/exhaust pipes to collect waste heat from industrial emission.

4.3. Curved thermoelectric device

Given that planar thermoelectric devices are not completely applicable to different scenarios, two 3D thermoelectric devices with different radians were designed. Fig. 7(a) shows the thermoelectric devices with a curved structure that can be implemented to a large curved heat source. Fig. 7(b) shows an annular thermoelectric device for a small heat source. The heat source was located in the middle, and the heat was radially transferred along the thermoelectric leg. The interrelated dimensions of the two thermoelectric devices are shown in Table 4. A single thermoelectric device was tested in the range of 323.15 K−398.15 K to verify its usage on a curved surface.

The internal resistance values of a single curved thermoelectric device and annular device were 17.5 Ω and 23.5 Ω at room temperature, respectively. At 398.15 K hot surface temperature, the V_{oc} and P_{max} of the curved thermoelectric device reached 265 mV and 948.5 μW, respectively; and those of the annular thermoelectric device reached 332.1 mV and 1.2 mW, respectively (Fig. 7(c−f)). The ΔT values of the two devices were 80.9 K and 86.4 K, respectively. The varied V_{OC} and P_{max} of the thermoelectric devices in relation to the hot surface temperature showed a positive correlation with ΔT. A single device had an electrical output close to or even exceeding the mW level under a low heat source condition. This result indicates that the 3D thermoelectric devices fabricated by the cold−press sintering and molding method have excellent practicability. Higher electrical performance of thermoelectric devices with system layout and series-parallel could be obtained by collecting the heat of wastewater and exhaust pipes design. Moreover, power supply device like radioisotope thermoelectric generators fabricated by curved thermoelectric devices will win a bright application prospect.

5. Conclusions

To achieve the sustainable application of low-quality heat, the high-performance and structure-adjustable 3D thermoelectric devices based on cold−press sintering and molding was innovatively fabricated by introducing ultralow thermal conductivity. This works effectively solve the communal problem with high breakage rate, small temperature difference, and poor practicality. The combined effect of the holes introduced by the binder and the pressurization process analyzed from the microstructure and transport properties reduced the thermal conductivity and enhanced the thermoelectric properties. The maximum ZT values of the pressurized P/N thermoelectric materials reached 1.09 and 0.5 at room temperature, which results in the much greater P_{max} of the pressurized thermoelectric devices than that of the unpressurized one under the same conditions. Fully-scaled 3D thermoelectric devices applicative were prepared in accordance with practical application requirements. At 398.15 K hot surface temperature, the small arrayed thermoelectric devices obtained V_{oc} and P_{max} of 584 mV and 627.7 μW, respectively; and the large arrayed thermoelectric devices obtained V_{oc} and P_{max} of 573.8 mV and 1.2 mW, respectively. In case of a surface heat source at 398.15 K hot surface temperature, the V_{oc} and P_{max} of the curved thermoelectric devices reached 265 mV and 948.5 μW, respectively; and those of the annular thermoelectric devices reached 332.1 mV and 1.2 mW, respectively. 3D thermoelectric devices have excellent practicability, which targets applications in heat reclaimer, solar−thermal

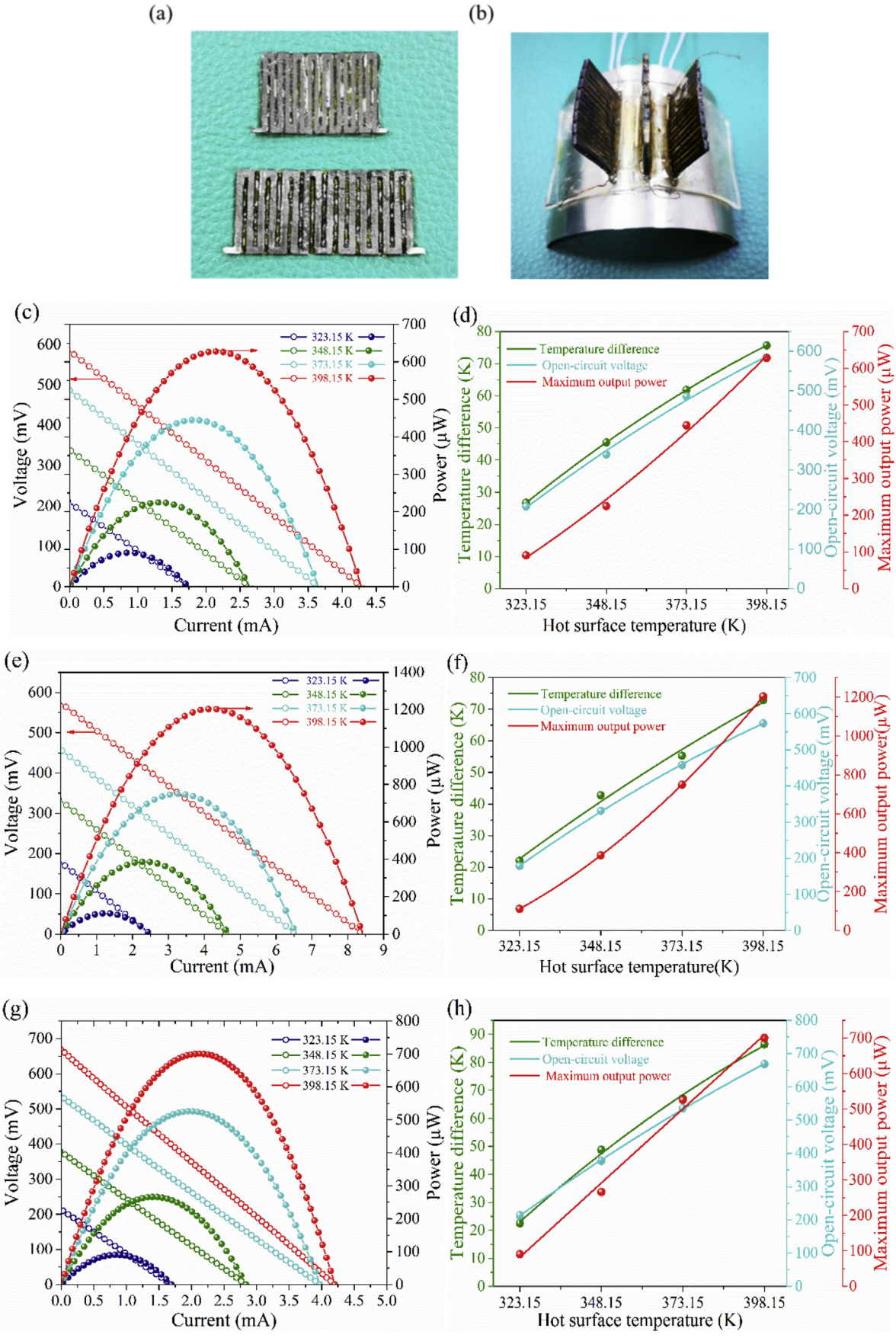

Fig. 6. Electrical performance of arrayed thermoelectric devices: (a) single thermoelectric device, (b) tandem of small thermoelectric devices on curved surface, (c) *I–V/I–P* characteristic curves and (d) ΔT, V_{oc}, and P_{max} vs. hot surface temperature of small thermoelectric devices, (e) *I–V/I–P* characteristic curves and (f) ΔT, V_{oc}, and P_{max} vs. hot surface temperature of large thermoelectric devices, (g) *I–V/I–P* characteristic curves and (h) ΔT, V_{oc} and P_{max} vs. hot surface temperature on curved surface.

Table 3
Relevant structural dimensions of two arrayed thermoelectric devices.

Type		Small size	Large size
Thermoelectric leg (mm^3)	Length (mm)	20	20
	Width (mm)	1	1.5
	Thickness (mm)	1.6	1.9
Number of thermoelectric legs (pair)		8	8
Overall dimensions (mm^3)		31 × 21 × 1.6	41 × 21 × 1.9

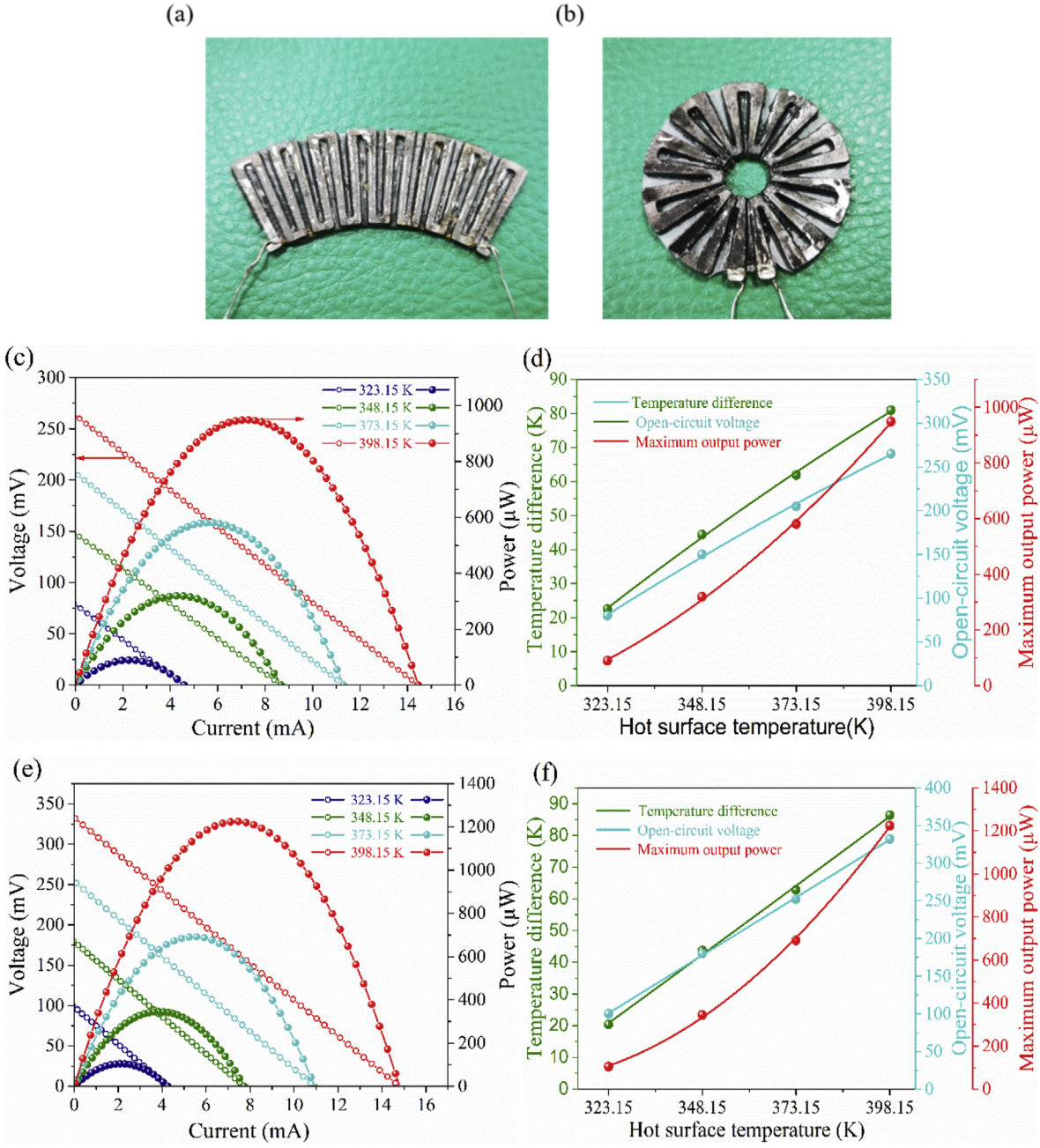

Fig. 7. Electrical performance of curved thermoelectric devices: (a) single curved thermoelectric device, (b) single annular thermoelectric device, (c) *I–V/I–P* characteristic curves and (d) ΔT, V_{oc}, and P_{max} vs. hot surface temperature of single curved thermoelectric device, (e) *I–V/I–P* characteristic curves and (f) ΔT, V_{oc}, and P_{max} vs. hot surface temperature of single annular thermoelectric device.

Table 4
Relevant structural dimensions of two curved thermoelectric devices.

Type		Curved type	Annular type
Thermoelectric leg (mm^3)	Radius (mm)	20	15.5
	Width (mm)	1.4–2.1	0.7–3.14
	Thickness (mm)	1.3	1.3
Radius of heat source (mm)		20	4
Number of thermoelectric legs (pair)		8	10

conversion system and radioisotope thermoelectric generator. The next works will comprehensively consider the influence of preparation parameters on the thermoelectric materials. Through deeply integrated design and assembly of the above thermoelectric devices, electronic components are expected to be powered in several areas.

CRediT authorship contribution statement

Kai Liu: Conceptualization, Methodology, Writing - original draft. **Xiaobin Tang:** Conceptualization, Writing - review & editing. **Yunpeng Liu:** Software, Writing - review & editing. **Zhiheng Xu:** Formal analysis, Writing - review & editing. **Zicheng Yuan:** Software, Visualization. **Zhengrong Zhang:** Resources.

Declaration of competing interest

The authors declare that they have no known competing financial interests or personal relationships that could have appeared to influence the work reported in this paper.

Acknowledgements

This work was supported by the Fundamental Research Funds for the Central Universities (Grant No. NP2018462), the Postgraduate Research & Practice Innovation Program of Jiangsu Province (Grant No. KYCX19_0176), the Short Visit Program of Nanjing University of Aeronautics and Astronautics (Grant No. 191104DF06).

Appendix A. Supplementary data

Supplementary data to this article can be found online at https://doi.org/10.1016/j.energy.2020.118096.

References

[1] He W, Zhang G, Zhang X, Ji J, Li G, Zhao X. Recent development and application of thermoelectric generator and cooler. Appl Energy 2015;143:1–25.
[2] Champier D. Thermoelectric generators: a review of applications. Energy Convers Manag 2017;140:167–81.
[3] Yang L, Chen Z, Dargusch MS, Zou J. High performance thermoelectric materials: progress and their applications. Adv. Energy Mater. 2018;8(6):1701797.
[4] Kraemer D, Jie Q, McEnaney K, Cao F, Liu W, Weinstein LA, et al. Concentrating solar thermoelectric generators with a peak efficiency of 7.4%. Nat Energy 2016;1:1–8.
[5] Guo Y, Dun C, Xu J, Li P, Huang W, Mu J, Hou C, Hewitt CA, Zhang Q, Li Y. Wearable thermoelectric devices based on Au-decorated two-dimensional MoS2. ACS Appl Mater Interfaces 2018;10(39):33316–21.
[6] Kong D, Zhu W, Guo Z, Deng Y. High-performance flexible Bi_2Te_3 films based wearable thermoelectric generator for energy harvesting. Energy 2019;175:292–9.
[7] Kempf N, Zhang Y. Design and optimization of automotive thermoelectric generators for maximum fuel efficiency improvement. Energy Convers Manag 2016;121:224–31.
[8] Zhu P, Wang Y, Sheng M, Wang Y, Yu Y, Deng Y. A flexible active dual-parameter sensor for sensitive temperature and physiological signal monitoring via integrating thermoelectric and piezoelectric conversion. J Mater Chem A 2019;7(14):8258–67.
[9] Feng R, Tang F, Zhang N, Wang X. Flexible, high-power density, wearable thermoelectric nanogenerator and self-powered temperature sensor. ACS Appl Mater Interfaces 2019;11(42):38616–24.
[10] Liu K, Tang X, Liu Y, Xu Z, Yuan Z, Li J, Zhang Z. Preparation and optimization of miniaturized radioisotope thermoelectric generator based on concentric filament architecture. J Power Sources 2018;407:14–22.
[11] Bahrami P, Nesmith B, Carpenter K. Milli-watt radioisotope power to enable small, long-term robotic "Probe" space exploration. In: IEEE aerosp. conf., IEEE; 2017; 2017. p. 1–8.
[12] Holgate TC, Bennett R, Hammel T, Caillat T, Keyser S, Sievers B. Increasing the efficiency of the multi-mission radioisotope thermoelectric generator. J Electron Mater 2015;44(6):1814–21.
[13] Wang Y, Shi Y, Mei D, Chen Z. Wearable thermoelectric generator to harvest body heat for powering a miniaturized accelerometer. Appl Energy 2018;215:690–8.
[14] Xu Z, Wu H, Zhu T, Fu C, Liu X, Hu L, He J, He J, Zhao X. Attaining high mid-temperature performance in (Bi, Sb) 2 Te 3 thermoelectric materials via synergistic optimization. NPG Asia Mater 2016;8(9):e302.
[15] Zou P, Xu G, Wang S. Thermoelectric properties of nanocrystalline Bi 2 (Te 1–x Se x) 3 prepared by high-pressure sintering. J Electron Mater 2015;44(6):1592–8.
[16] Zhang Q, Zhou Z, Dylla M, Agne MT, Pei Y, Wang L, Tang Y, Liao J, Li J, Bai S. Realizing high-performance thermoelectric power generation through grain boundary engineering of skutterudite-based nanocomposites. Nanomater Energy 2017;41:501–10.
[17] Zhang Q, Liao J, Tang Y, Gu M, Ming C, Qiu P, Bai S, Shi X, Uher C, Chen L. Realizing a thermoelectric conversion efficiency of 12% in bismuth telluride/skutterudite segmented modules through full-parameter optimization and energy-loss minimized integration. Energy Environ Sci 2017;10(4):956–63.
[18] Aranguren Garacochea P, Astrain Ulibarrena D, Rodríguez García A, Martínez Echeverri Á. Experimental investigation of the applicability of a thermoelectric generator to recover waste heat from a combustion chamber. Appl Energy 2015;152:121–30.
[19] Feng J, Zhu W, Deng Y, Song Q, Zhang Q. Enhanced antioxidation and thermoelectric properties of the flexible screen-printed Bi2Te3 films through interface modification. ACS Appl Energy Mater 2019;2(4):2828–36.
[20] Kim YJ, Kim SJ, Choi H, Kim CS, Lee G, Park SH, Cho BJ. Realization of high-performance screen-printed flexible thermoelectric generator by improving contact characteristics. Adv. Mater. Interfaces 2017;4(23):1700870.
[21] Varghese T, Hollar C, Richardson J, Kempf N, Han C, Gamarachchi P, Estrada D, Mehta RJ, Zhang Y. High-performance and flexible thermoelectric films by screen printing solution-processed nanoplate crystals. Sci Rep 2016;6:33135.
[22] Choi H, Kim SJ, Kim Y, We JH, Oh MW, Cho BJ. Enhanced thermoelectric properties of screen-printed Bi0.5Sb1.5Te3 and Bi2Te2.7Se0.3 thick films using a post annealing process with mechanical pressure. J Mater Chem C 2017;5(33):8559–65.
[23] Choi H, Kim YJ, Kim CS, Yang HM, Oh MW, Cho BJ. Enhancement of reproducibility and reliability in a high-performance flexible thermoelectric generator using screen-printed materials. Nanomater Energy 2018;46(December 2017):39–44.
[24] Perez-Taborda JA, Vera L, Caballero-Calero O, Lopez EO, Romero JJ, Stroppa DG, et al. Pulsed hybrid reactive magnetron sputtering for high zT Cu2Se thermoelectric films. Adv Mater Technol 2017;2:1700012.
[25] Xu Z, Li J, Tang X, Liu Y, Jiang T, Yuan Z, Liu K. Electrodeposition preparation and optimization of fan-shaped miniaturized radioisotope thermoelectric generator. Energy 2020;194:116873.
[26] He M, Zhao Y, Wang B, Xi Q, Zhou J, Liang Z. 3D printing fabrication of amorphous thermoelectric materials with ultralow thermal conductivity. Small 2015;11(44):5889–94.
[27] Kim F, Kwon B, Eom Y, Lee JE, Park S, Jo S, Park SH, Kim BS, Im HJ, Lee MH. 3D printing of shape-conformable thermoelectric materials using all-inorganic Bi2Te3-based inks. Nat. Energy 2018;3.
[28] Jo S, Choo S, Kim F, Heo SH, Son JS. Ink processing for thermoelectric materials and power-generating devices. Adv. Mater. 2019;31(20):1–16.